Crustal seismic anisotropy along the continental margin in western Canada from receiver function analysis

T. Tracey Kyryliuk[1], P. Audet[1], J. M. Gosselin[1,2], and A. J. Schaeffer[3]

[1]Department of Earth and Environmental Science, University of Ottawa, Ottawa, ON, K1N 6N5

[2]Now at Department of Geoscience, University of Calgary, Calgary, AB, T2N 1N4

[3]Geological Survey of Canada, Natural Resources Canada, Sidney, BC, V8L 4B2

Key Points:

- Receiver functions are calculated for 74 broadband 3-component seismic stations across coastal British Columbia.
- We detect signs of seismic anisotropy beneath all stations in our study.
- Seismic anisotropy is attributed to changes in Moho depth, faults, and pervasive deformation-related fabrics.

Corresponding author: T. Tracey Kyryliuk, ttrac015@uottawa.ca

Abstract

Coastal British Columbia, Canada, has the highest seismic hazard in the country due to convergent and transpressive deformation at offshore plate boundaries between the Pacific, Juan de Fuca and North American plates. Further landward, the crust of the North American plate is made up of several geologically unique terranes and is unusually thin. Investigating the geophysical features in this area can help us better constrain its tectonic history and the geophysical processes that are currently underway. Here, we conduct an analysis of teleseismic body-wave scattering data (i.e, receiver functions) recorded at stations across western coastal British Columbia including northern Vancouver Island and southeastern Alaska. Using these receiver functions, we perform a harmonic decomposition with respect to earthquake back-azimuths to determine the orientation of seismic anisotropy over a series of depth ranges, attributable to either mineral alignment or dipping structures. We find a coherent pattern of margin-parallel orientations at upper crustal depths that persist onto the mainland at distances 420 km from the margin. Furthermore, dominant receiver function orientations at depth are attributed to dipping faults and interfaces, and fabrics due to lower crustal shearing or inherited from tectonic assembly along the margin. This work provides insight into the evolution of the margin and surrounding region, as well as the tectonic processes currently taking place. Identification of the dipping interfaces associated with the subducting Pacific and Juan de Fuca plates is important for assessment of earthquake and tsunami hazards.

Plain Language Summary

Coastal British Columbia is a geologically complex region, but could it also be the epicenter of large tsunami causing earthquakes that put the lives of residents all around the Pacific at risk? Better understanding how this region formed and the current geometry of the tectonic plates can help us address this question. We study seismic waves from distant earthquakes recorded at over 60 seismometers distributed across western British Columbia to see if wave speeds depend on the direction from which the earthquake approaches. This directional dependence could be caused by a dipping boundary between two different media in the Earth's crust/mantle or by a directional dependence in properties of the material the wave travels through. We detect directional dependency in seismic wave speeds beneath all seismometers in our study at multiple depths in the Earth's crust/uppermost mantle. From this data set we determine the strike of dipping bound-

aries and/or the trend of material properties, coming from various sources such as changes in the thickness of the crust, faults, and material fabrics caused by deformation. Results of this study add to the body of knowledge of the formation history of western British Columbia and the assessment of earthquake and tsunami hazards.

1 Introduction

The continental margin of British Columbia (BC), in western Canada, is a geologically complex region due to its tectonic history and modern tectonic regime. This region is currently characterized by a plate boundary system that transitions from subduction in the south to transform motion in the north. On Vancouver Island, the Cascadia subduction zone defines underthrusting of the the Juan de Fuca (JdF) plate beneath the North American (NA) plate. North of the Cascadia subduction zone, the region is comprised of a poorly defined and evolving triple junction between NA, the Pacific (PA) plate and the Explorer (Ex) microplate. Further north, the plate boundary between PA and NA evolves into the dextral transform Queen Charlotte Fault (QCF). The Haida Gwaii archipelago marks the transition between the triple junction and the transform system, although the exact nature of the boundary between the PA and NA plates in this region remains ambiguous (Hyndman & Ellis, 1981; Rohr et al., 2000; Smith et al., 2003; ten Brink et al., 2018). Currently, there is non-zero convergence of ∼15 mm/year between the two plates due to the transpressive nature of the margin along the restraining southern part of the QCF (DeMets & Dixon, 1999; DeMets et al., 2010; Schoettle-Greene et al., 2020). Seismic, thermal and other geophysical evidence suggest that the convergence is accommodated by oblique underthrusting of the PA plate beneath Haida Gwaii (Smith et al., 2003; Bustin et al., 2007; Lay et al., 2013; Gosselin et al., 2015; Hyndman, 2015; ten Brink et al., 2018). The landward extent of underthrusting of the PA plate beneath NA is currently unknown (Smith et al., 2003; ten Brink et al., 2018); resolving this question is important for seismic hazard and tectonic reconstruction models.

Further landward, the geology changes relatively little along the strike of the margin (Monger, 1993) but from west to east, the mainland is characterized by a collage of accreted and deformed exotic terranes. These terranes are grouped into two superterranes defined by two accretionary episodes and are separated by the margin-parallel crustal scale Coast Shear Zone (CSZ). The Coast Plutonic Complex (CPC) was intruded into

this shear zone during long-lived subduction-related arc magmatism and exhumation along the margin (Hollister & Andronicos, 2006). The surficial geology of this region is relatively well studied (Nelson et al., 2007, 2013) and efforts have been made to constrain its crustal structure and fabrics by means of geophysical data (Hammer et al., 2000; Morozov et al., 2001; Hollister & Andronicos, 2006; Calkins et al., 2010). Results of these studies show that the Moho dips from west to east to a depth of up to 37 km beneath the easternmost terrane (inland) and the mantle-lithosphere boundary is between 60-70 km depth (Hollister & Andronicos, 2006; Calkins et al., 2010).

Seismic anisotropy is the directional dependence of seismic wave propagation, and is one of the best tools to study the structure and fabrics of the crust (Babuska & Cara, 1991). In particular, anisotropy characterized using teleseismic receiver functions (RFs) can be used to constrain the geometry and seismic velocities across dipping interfaces, and/or rock fabrics from large-scale mineral alignment in the crust (e.g., Levin & Park, 1997; Savage, 1998a). The goal of this paper is to use RFs to investigate variations in seismic anisotropy along the continental margin of BC. In particular, we use RFs to search for evidence of dipping structures or material anisotropy at a range of crustal depths, and interpret these observations in relation to modern and past geodynamic environments.

A handful of studies have previously examined crustal structure using RFs in western Canada, although none of them considered the broader context of the entire continental margin. Notably, RFs were used to study the extent of subduction beneath northern Cascadia (Audet et al., 2008), underthrusting beneath Haida Gwaii (Smith et al., 2003; Bustin et al., 2007; Gosselin et al., 2015), and the architecture of the crust across the CPC (Calkins et al., 2010). However, these studies did not examine back-azimuth (BAZ) variations in RF signals and therefore could not resolve seismic anisotropy. Lastly, significant expansion of regional seismic networks in this area occurred following the moment-magnitude 7.8 thrust earthquake and associated tsunami off the west coast of Haida Gwaii in 2012 (Cassidy et al., 2014; Leonard & Bednarski, 2014), further motivating additional RF studies in the region.

Other previous seismic studies of crustal structure and fabrics include local shear-wave splitting on Haida Gwaii (Cao et al., 2017) and southern Vancouver Island and surrounding area (Balfour et al., 2012), surface wave tomography (Gosselin et al., 2020), and seismic reflection along the Portland Canal in BC (Morozov et al., 1998). We use

observations and conclusions from these past studies to interpret our own results in light of the dominant orientations of previously recognized geological and geophysical features. We also consider how these features evolve landward from the Haida Gwaii margin and as a function as depth. These results give further insight into the past and present tectonic regime of the Haida Gwaii margin and surrounding geological units.

2 Tectonic Setting and History

The tectonics of the Cordillera in western Canada throughout the Mesozoic are dominated by the interactions between the now defunct Kula and Farallon plates with the PA and NA plates (Engebretson et al., 1984; ten Brink et al., 2018). The continent-ocean boundary is considered to have initiated in the late Proterozoic and continued to evolve throughout the Phanerozoic (Monger, 1993). Our particular study area is comprised of five geomorphologically distinct regions from west to east: the Wrangellia terrane, the Alexander terrane, the Yukon-Tanana terrane (YTT) (also sometimes referred to as Taku), the CPC and the Stikinia terrane. Continental growth by accretion of the terranes likely occurred in two episodes (Gabrielse et al., 1991). First, the Intermontane superterrane, which includes Stikinia and YTT, is believed to have thrust eastward onto the NA plate during dextral transpression some time during the Jurassic (Hammer et al., 2000). Next, the Insular superterrane, containing the Wrangellia and Alexander terranes, is believed to have been thrust onto the NA plate during sinistral transpression in the mid-Cretaceous (Chardon et al., 1999; Hammer et al., 2000). This second accretionary episode is also considered a contributor to deformation of the Intermontane superterrane (Hammer et al., 2000).

The result of the proposed history of large-scale transpression along western NA is a juxtaposition of distinct crustal materials separated by shear zones and northwest striking crustal scale fault systems (Chardon et al., 1999; ten Brink et al., 2018). A mid-Cretaceous thrust belt west of the CPC extends from the surface down to the mantle (Hollister & Andronicos, 2006). This feature is expressed as an offset in Moho depth (Hollister & Andronicos, 2006; Calkins et al., 2010).

Concurrent with the transpressive motion, prolonged subduction of the Kula-Farallon plate system under NA would have generated a continental magmatic arc in the shear zone between the two superterranes, possibly in two episodes (Engebretson et al., 1984;

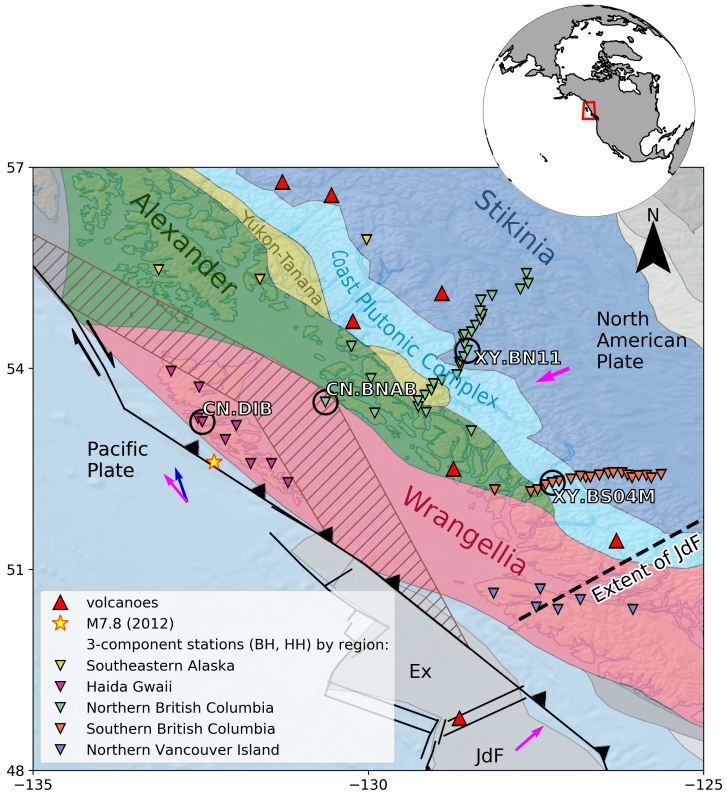

Figure 1. Map of the study area. The estimated absolute and relative motions of the plates are shown as colored vectors, based on the Hotspot reference frame (magenta) and relative to NA (blue) (Gripp & Gordon, 2002). The brown hatched polygon outlines the possible landward extent of the subducted PA slab (Smith et al., 2003). Dashed line shows the approximate northern terminus of JdF plate subduction (Savard et al., 2020). Stations are colour-coded by regional sets. Stations with RF analysis shown in subsequent figures are circled and labeled. The epicentre of the 2012 earthquake is marked with a star. Terranes relevant to this study are highlighted and labelled by colour.

Calkins et al., 2010; ten Brink et al., 2018). During the first episode, subduction related partial melting and mixing would have resulted in the emplacement of plutons within the shear zone (Hollister & Andronicos, 2006). The relative change in plate motions in the early Eocene would then have caused a period of crustal extension, moving the upper crust of the shear zone onto Stikinia and exhuming the plutons, creating the CPC (Hollister & Andronicos, 2006) and forming a northeast foliated, northeast dipping, ductile shear zone on the eastern boundary between the CPC and Stikinia (Andronicos et

al., 2003). Several of these felsic plutons within the CPC appear to be sill-like or domed in shape (Hollister & Andronicos, 2006).

Eventual subduction of the spreading ridge between the Kula and Farallon plates would have then led to the development of a slab window, well established by the early Miocene and believed to currently encompass southeastern Alaska to southwest BC (Thorkelson & Taylor, 1989). This slab window is linked with the generated intraplate volcanism within a hot and thin lithosphere (Thorkelson et al., 2011). It is suggested that the Kula plate was captured by the PA early-mid Eocene and began the predominantly right-lateral motion seen today along the QCF (ten Brink et al., 2018). Upon complete subduction of the ridge, the triple junction between the PA, NA plates and JdF plate (the remnant of the Farallon plate) would have moved south to its current location (Thorkelson & Taylor, 1989).

The modern configuration of tectonic plates is shown in Figure 1. The continental margin of NA extends to the western coast of Haida Gwaii, where it meets the PA near the dextral transform QCF, which is among Canada's most seismically active regions (Hyndman & Ellis, 1981; Bird, 1999). To the north, the QCF transitions into the Fairweather Fault in southeastern Alaska. The NA-PA-Ex triple junction is poorly defined and is situated somewhere between the northern end of Vancouver Island and southern Haida Gwaii (Savard et al., 2020). The Ex plate accommodates the relative motions of the NA, PA and JdF plates and its separation from the JdF plate is attributed to thermomechanical erosion of the slab edge and thining of the slab (Audet et al., 2008). To the south of the triple junction, subduction of the JdF plate beneath NA defines the Cascadia subduction zone. Above this portion of the subduction zone, clockwise rotation of the Oregon block drives the west coast of the United States northward (McCaffrey et al., 2000; Balfour et al., 2012).

Along Haida Gwaii, the motion of the PA plate relative to NA is 338° clockwise from north. The direction of plate motion with respect to the orientation of the margin (Fig. 1) results in convergence of $\sim$15 mm yr^{-1} (Gripp & Gordon, 2002), which is accommodated by either crustal thickening or oblique subduction of the PA slab beneath NA (Smith et al., 2003). In 2012, a M_W=7.8 earthquake with a dominant thrust component occurred at the Haida Gwaii margin (Cassidy et al., 2014), confirming that the plate boundary fault dips beneath Haida Gwaii. Plate kinematics place the landward

extent of potential underthrusting of the PA plate beneath Hecate Strait (east of Haida Gwaii; Figure 1). However, the exact limit depends on the time of subduction initiation as well as the location of the triple junction at that time (Smith et al., 2003), both of which are uncertain. Seismic evidence of the downward extent of the PA slab is limited (Bustin et al., 2007; Gosselin et al., 2015, 2020), and the extent of possible subduction is currently unresolved.

3 Methodology

3.1 Receiver functions

At teleseismic distances, direct P-waves from moderate (magnitude M >5.5) earthquakes arrive before any other body-wave phase, and can be approximated as a nearly vertically propagating plane wave incident beneath a recording station. The incoming P wave interacts with subsurface seismic velocity discontinuities and produces P-to-S converted phases that are projected onto the horizontal components of motion. By approximating the vertical-component P-wave seismogram as a source wavelet incident on the receiver-side structure, we can deconvolve it from the horizontal components and produce a so-called RF that isolates the P-to-S conversions. Consequently, RFs are approximations to the Earth's impulse response, and provide a valuable constraint on one-dimensional seismic velocity structure beneath a seismic station (Langston, 1977, 1979; Cassidy, 1992; Savage, 1998b). The timing of the phases in the RF can be used to infer the depth of the seismic velocity discontinuities that produced them, and the amplitudes of the phases can be used to infer the magnitude of the contrast in seismic velocities across the discontinuities.

For a horizontally layered isotropic medium, P-to-S converted energy is constrained to the radial plane (i.e., in line with the distant earthquake). However, in the presence of dipping layers and/or material anisotropy, P-to-S converted energy can be projected out of the radial plane and onto the transverse component of motion. Consequently, the presence of coherent arrivals on transverse-component RFs is indicative of dipping structure and/or material anisotropy beneath a seismic station (Cassidy, 1992; Savage, 1998b). The amplitude, polarity and timing of RF phases vary smoothly with respect to the BAZ of the event used to produce the RF (Porter et al., 2011). This directional dependence can be used to infer the geometry and orientation of complex subsurface structure by

modelling sinusoidal variations in RF phases (e.g., Bianchi et al., 2010; Porter et al., 2011; Schulte-Pelkum & Mahan, 2014; Audet, 2015).

3.2 Harmonic decomposition

In this work, we decompose the RF data at each station into low-order periodic functions (i.e., harmonics). Specifically, a set of N radial R_V and transverse R_T RFs at a given station can be decomposed into five harmonic components according to:

$$\begin{pmatrix} R_{V1}(z) \\ \vdots \\ R_{VN}(z) \\ R_{T1}(z) \\ \vdots \\ R_{TN}(z) \end{pmatrix} = \begin{pmatrix} 1 & \cos(\phi_1-\alpha) & \sin(\phi_1-\alpha) & \cos(2(\phi_1-\alpha)) & \sin(2(\phi_1-\alpha)) \\ \vdots & & & & \\ 1 & \cos(\phi_N-\alpha) & \sin(\phi_N-\alpha) & \cos(2(\phi_N-\alpha)) & \sin(2(\phi_N-\alpha)) \\ 0 & \cos(\phi_1-\alpha+\frac{\pi}{2}) & \sin(\phi_1-\alpha+\frac{\pi}{2}) & \cos(2(\phi_1-\alpha)+\frac{\pi}{4}) & \sin(2(\phi_1-\alpha)+\frac{\pi}{4}) \\ \vdots & & & & \\ 0 & \cos(\phi_N-\alpha+\frac{\pi}{2}) & \sin(\phi_N-\alpha+\frac{\pi}{2}) & \cos(2(\phi_N-\alpha)+\frac{\pi}{4}) & \sin(2(\phi_N-\alpha)+\frac{\pi}{4}) \end{pmatrix} \begin{pmatrix} A(z) \\ B_\parallel(z) \\ B_\perp(z) \\ C_\parallel(z) \\ C_\perp(z) \end{pmatrix}, \tag{1}$$

where ϕ_i is the BAZ of the i-th event. The harmonic term A is the mean of the radial component RFs, and represents the signal in the data due to isotropic structure. $B_\parallel$ and $B_\perp$ are the first harmonic terms, and describe signal in the RF dataset that varies with 2-π periodicity over BAZ, which has been shown to be attributed to dipping interfaces and anisotropic materials with a plunging axis of hexagonal symmetry (e.g., Porter et al., 2011; Schulte-Pelkum & Mahan, 2014). Similarly, $C_\parallel$ and $C_\perp$ correspond to signals that arise from anistropic materials with a horizontal axis of symmetry, which display a π periodicity in RFs (Bianchi et al., 2010; Audet, 2015). Unfortunately, the ability to accurately constrain these higher-order harmonic terms is typically limited by the azimuthal sampling of the RF dataset. However, we note in Equation 1 the predicted azimuthal shift for the transverse component relative to the radial component, which has the effect of improving the azimuthal coverage.

Note that R_V and R_T represent the time-to-depth converted radial and transverse components, respectively. We discuss the depth conversion processing further below. Lastly, α represents the rotation angle of the harmonic reference frame. In a geographic reference frame ($\alpha = 0$), the coordinate system of the BAZ harmonics is aligned with the north-south and east-west directions (Bianchi et al., 2010). Instead, an angle α that maximizes signal variance on a specific harmonic component can be estimated in order to infer the alignment of structural features beneath a seismic station (Audet, 2015). In this work, we estimate α by maximizing signal on the $B_\perp$ component. Under this frame ro-

tation, α represents the strike of a dipping layer or the trend of a dipping orientation in anisotropic rocks (Audet, 2015).

3.3 Data processing

Our dataset comprises 74 broadband, 3-component seismograph stations distributed over Haida Gwaii, southeastern Alaska, northern Vancouver Island, and coastal BC (up to ~420 km landward) (Fig. 1). We separate coastal BC into southern and northern portions. These five regions are used to group RF results to describe regional structure.

We calculate RFs for all available data from earthquakes with moment magnitude greater than 5.8 during operation time of the stations. We use the iasp91 velocity model (Kennett & Engdahl, 1991) to download 120 second seismograms centered on the predicted P, or PP, arrival. We consider events over 30 - 90° and 100 - 160° degrees in epicentral distance for P and PP arrivals, respectively. We calculate the signal-to-noise (SNR) ratio relative to pre-arrival noise over the initial 30 s following the predicted arrival on the vertical component, filtered over the frequency range 0.05 - 1.0 Hz. We only consider data with SNR above 5.0 dB for further analysis. Next, we rotate the horizontal components to radial and transverse orientations relative to event locations (i.e., BAZ). RFs are then calculated using the multi-taper method in order to deconvolve the vertical component from the horizontal components (Park & Levin, 2000). The resulting high-quality RFs are then band-pass filtered between 0.05 and 0.8 Hz, binned by slowness and BAZ, and then migrated to depth using a 1D seismic velocity model provided by the Geological Survey of Canada (Canadian Hazards Information Service, 2021). This initial binning is performed in order to improve the computational efficiency of the depth migration. Subsequently, the depth-migrated RFs are binned into 72 BAZ bins. Lastly, we visually inspect the RF data at each station. Those that exhibit RF data with significant and/or uncharacteristic noise, or contain significant azimuthal gaps in data coverage (less than 50° of coverage), are not considered for further analysis.

For each station, we perform a harmonic decomposition in order to estimate the α parameter (equation 1) that minimizes the variance on the $B_{\parallel}$ harmonic component (i.e., maximizes variance on $B_{\perp}$) over a specific depth range for which we assume α to be constant. We perform this analysis for several overlapping depth ranges that are 10 km thick, from 5 to 50 km with a 5 km overlap. Previous studies suggest shallow Moho depths

of ∼32 km over much of western BC (Cook et al., 2010; Tarayoun et al., 2017), and 18-26 km beneath Haida Gwaii (Gosselin et al., 2015). Our analysis investigates structure through the entire crust. However, minimizing the $B_{\parallel}$ variance over 10 km-thick depth windows reduces the vertical resolution of our results. Lastly, we perform bootstrap re-sampling of the RF data at each station, and repeat the harmonic analysis for each bootstrap sample, in order to estimate $1-\sigma$ uncertainty on our estimated α values. Results with uncertainty greater than 36° are not considered in our interpretations.

4 Results

4.1 Examples at single stations

Figure 2 shows examples of RF processing and harmonic analysis for stations located on Haida Gwaii (DIB), southern BC (BS04M), northern BC (BN11) and Hecate Strait (BNAB) (Fig. 1). All stations display a gap in the RF coverage between 180° and 220° BAZ due to the paucity of global earthquakes at those BAZ. Stations DIB and BNAB have accumulated several years of high-quality data and display excellent coverage in BAZ. Stations BN11 and BS04M are part of a temporary network and display a sparser coverage in BAZ with significant gaps between 40° and 120°, due to their limited deployment duration. At all stations, we find periodic variations in amplitude with BAZ in both the radial and transverse components of RFs, which are indicative of seismic anisotropy and/or dipping structure beneath these stations (e.g., Fig. 2).

Figure 3 shows the harmonic components for stations DIB (a) and BNAB (b). For these examples, the angle α (equation 1) and the resulting components are calculated and shown for a selected depth range that encompasses the largest amplitude of the RF signals. Note the minimization of signal variance on the $B_{\parallel}$ components within the specific depth range, and the corresponding large signal variance on the $B_{\perp}$ components. Solving for α, as well as the corresponding signal variance on the $B_{\perp}$ component, over various depth ranges allows us to infer changes in the alignment and relative signal strength of dipping structure or anisotropy beneath a seismic station as a function of depth. The magnitude of the variance on $B_{\perp}$ represents the relative strength of anisotropic and/or dipping structures over the specified depth range, for the estimated orientation (Audet, 2015). For station DIB (Fig. 3(a)), there is large variance on the $B_{\parallel}$ component but offset in depth from $B_{\perp}$ indicating the presence of multiple sources with different orienta-

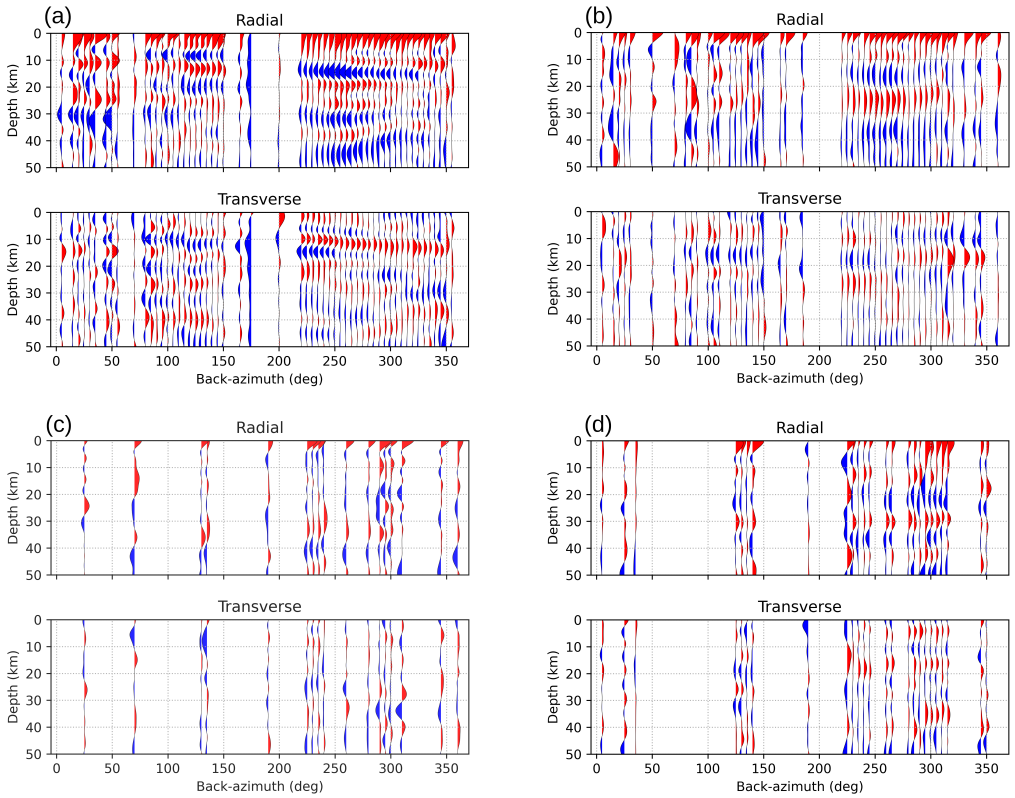

Figure 2. Examples of RF at stations DIB (a), BNAB (b), BN11 (c) and BS04M (d). These stations are circled and labelled in Figure 1. Radial (top panel) and transverse (bottom panel) RFs in each case are plotted from 0 to 50 km depth and sorted in BAZ bins.

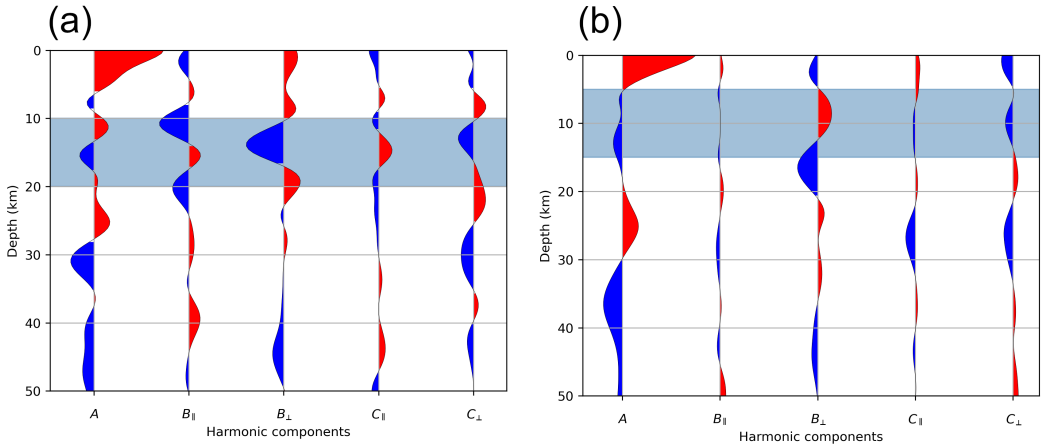

Figure 3. Examples of harmonic component analysis at corresponding stations DIB with $\alpha = 2 \pm 5°$ (a) and BNAB with $\alpha = 332 \pm 4°$ (b) in Figure 2. The decomposition is performed at the azimuth which minimizes the variance of the $B_\parallel$ component within the depth range highlighted by the grey shading. The five components are plotted from 0 to 50 km depth. Note the greater signal variance on the $B_\perp$ component within the shaded depth range.

tions contributing to this signal. Although the C components are also estimated and provide some constraint on azimuthal anisotropy, accurate estimation of these components requires greater RF data coverage over event BAZ (as discussed previously). Since such azimuthal coverage is highly variable between stations considered in this work due to differences in geographic location and station deployment duration, we do not consider the C components further.

4.2 Spatial variations

We map the spatial distribution of α for each 10 km depth range as oriented bars scaled by the magnitude of the variance on the $B_{\perp}$ component, and show the error in α as shaded bow ties (Fig. 4). At this scale, we observe a general NW-SE alignment at some depth ranges that follows the trend of terrane boundaries, but no obvious clustering of α by terrane (Fig. S1). Instead of examining results for separate geological units, we group results into the regional sets shown in Figure 1: southeastern Alaska, Haida Gwaii, northern BC, southern BC and northern Vancouver Island. These results are displayed as density estimates for the magnitude, orientation (azimuth difference with the PA plate motion) and standard deviation estimated for each depth range (Fig. 5).

Within the depth range of 5 - 15 km (Fig. 4(a)), α estimates are consistently oriented NW-SE over the entire region, with the overall magnitude of the signals being larger and more narrowly distributed than any other depth range. This is in general agreement with the strike of terrane boundaries and the directions of both the absolute and relative PA plate motion (Gripp & Gordon, 2002; Kreemer et al., 2014). Using rose diagrams, we determine the dominant RF orientations at this depth range and show the mean and standard deviation of α for the entire dataset and for each sub-region (Fig. 6). Comparing the sub-regions for this depth range from SE to NW (Fig. 4(a)), we observe a slight rotation in the orientation from 338° beneath northern Vancouver Island and southern BC to ∼320° beneath Haida Gwaii and northern BC, and then to 353° beneath southeastern Alaska.

Below the 5 - 15 km depth range, α values on the mainland exhibit complex patterns, with some locally coherent orientations. In southeastern Alaska, α values are rotated ∼30° clockwise from the PA plate motion within the 35 - 45 km depth range. Estimated α values beneath Haida Gwaii switch orientations between different depth ranges.

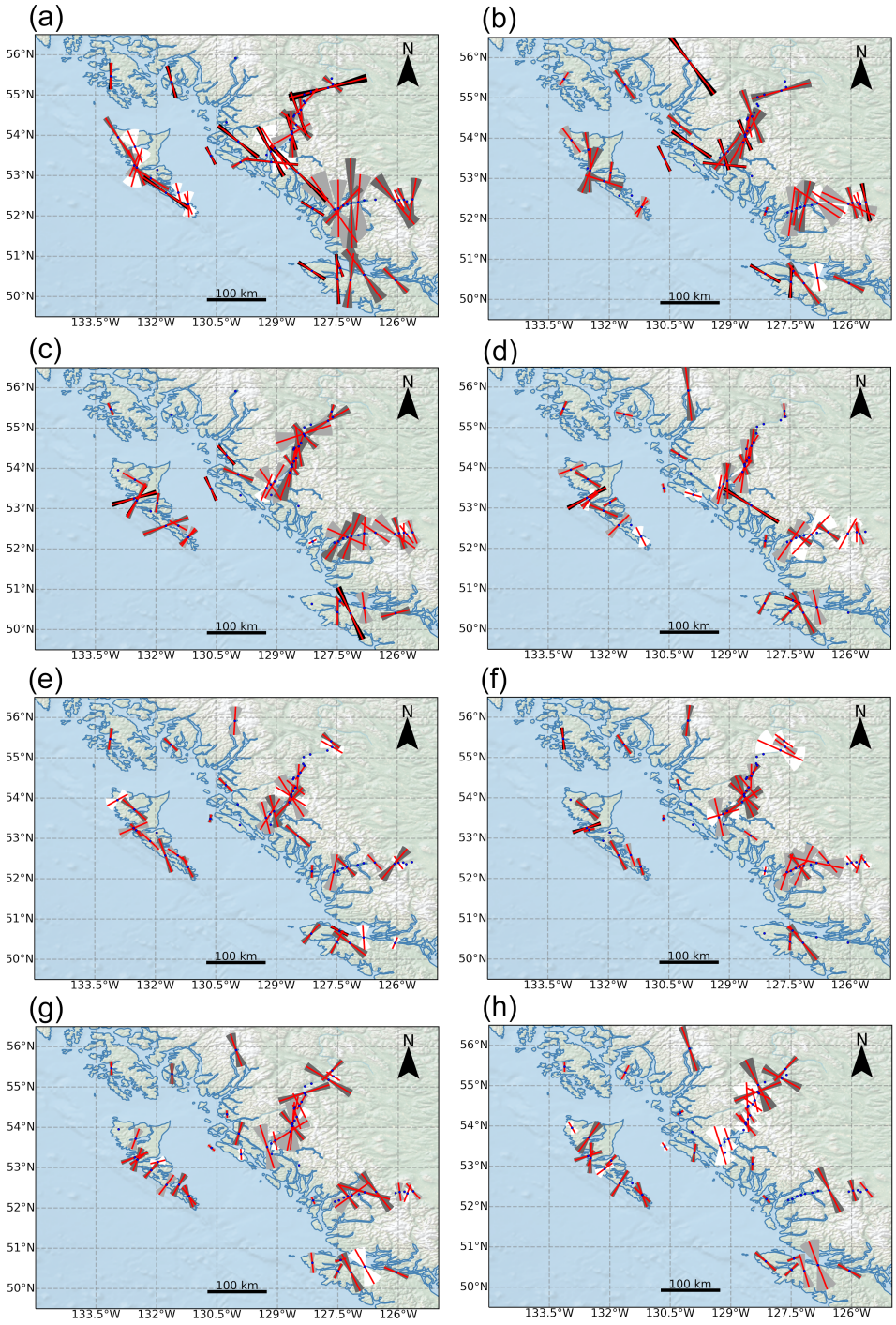

Figure 4. Maps of RF anisotropy for depth ranges of 5-15 km (a), 10-20 km (b), 15-25 km (c), 20-30 km (d), 25-35 km (e), 30-40 km (f), 35-45 km (g), and 40-50 km (h). The red bars show the orientation of the α estimates, which represent the strike of dipping structure or the trend of a plunging axis of hexagonal anisotropy. The red bars are scaled relative to the variance of the $B_\perp$ component over the corresponding depth range. The bowties show the 1 $-$ σ uncertainty, shaded by magnitude, darker shading indicates smaller uncertainty.

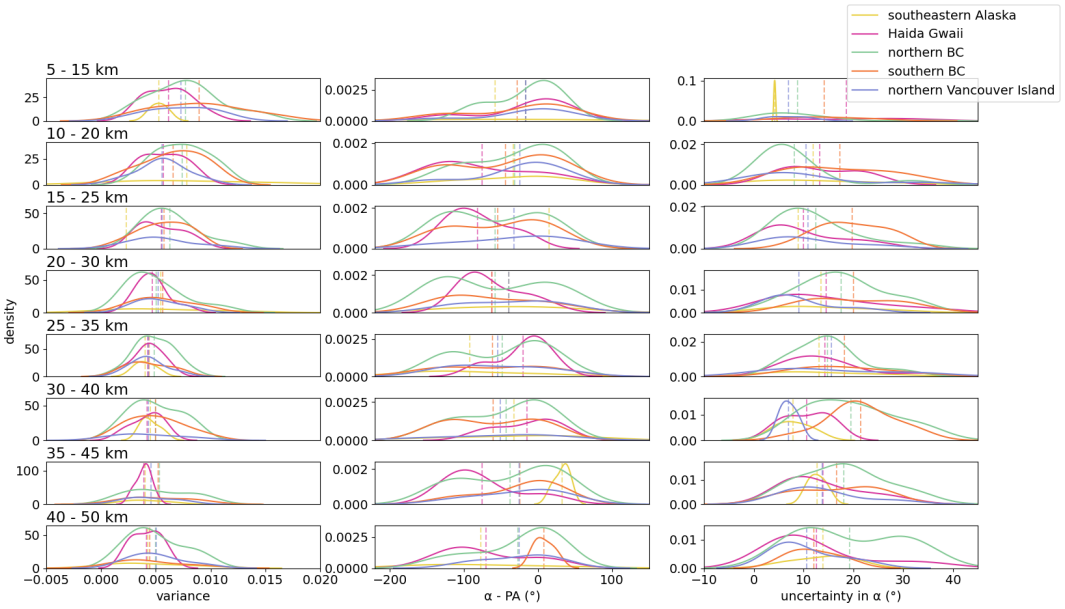

Figure 5. Plot showing the kernel density estimates of the $B_\perp$ component variance, angular difference between PA plate motion and α, and the angular uncertainty on α. Plots are colored according to station sub-region, and are ordered by increasing depth. Mean values for each sub-region are plotted as vertical dashed lines.

At shallow depths, orientations are sub-parallel to PA plate motion, then transition to sub-perpendicular (Fig. 5). Below 25 km, α values for the northern and southern BC groups have higher uncertainties due to a lower azimuthal coverage in the RF data at these stations compared to stations from permanent networks (Fig. 4). These regions also exhibit a broader distribution in α (Fig. 5). In general, the northern BC subset displays the most variability in dominant RF orientations (Fig. 5). Only for the depth range of 20 - 30 km do we see a coherent signal in this sub-region where the majority of the α estimates align approximately N-S. The overall trend in α values on northern Vancouver Island do not vary significantly across different depth ranges and show a NNW-SSE orientation (0-45 degrees clockwise from the PA plate motion).

In general, relative magnitudes in the measured seismic anisotropy (i.e., the variance of $B_\perp$, shown by the red bars in Figure 4 are large at all depth ranges considered, but are greatest for the shallower depth ranges (Fig. 5). Magnitudes are the smallest on the mainland and northern Vancouver Island for the 25 - 35 km depth range, and smallest on Haida Gwaii for the 35 - 45 km depth range. Stations further inland tend to have

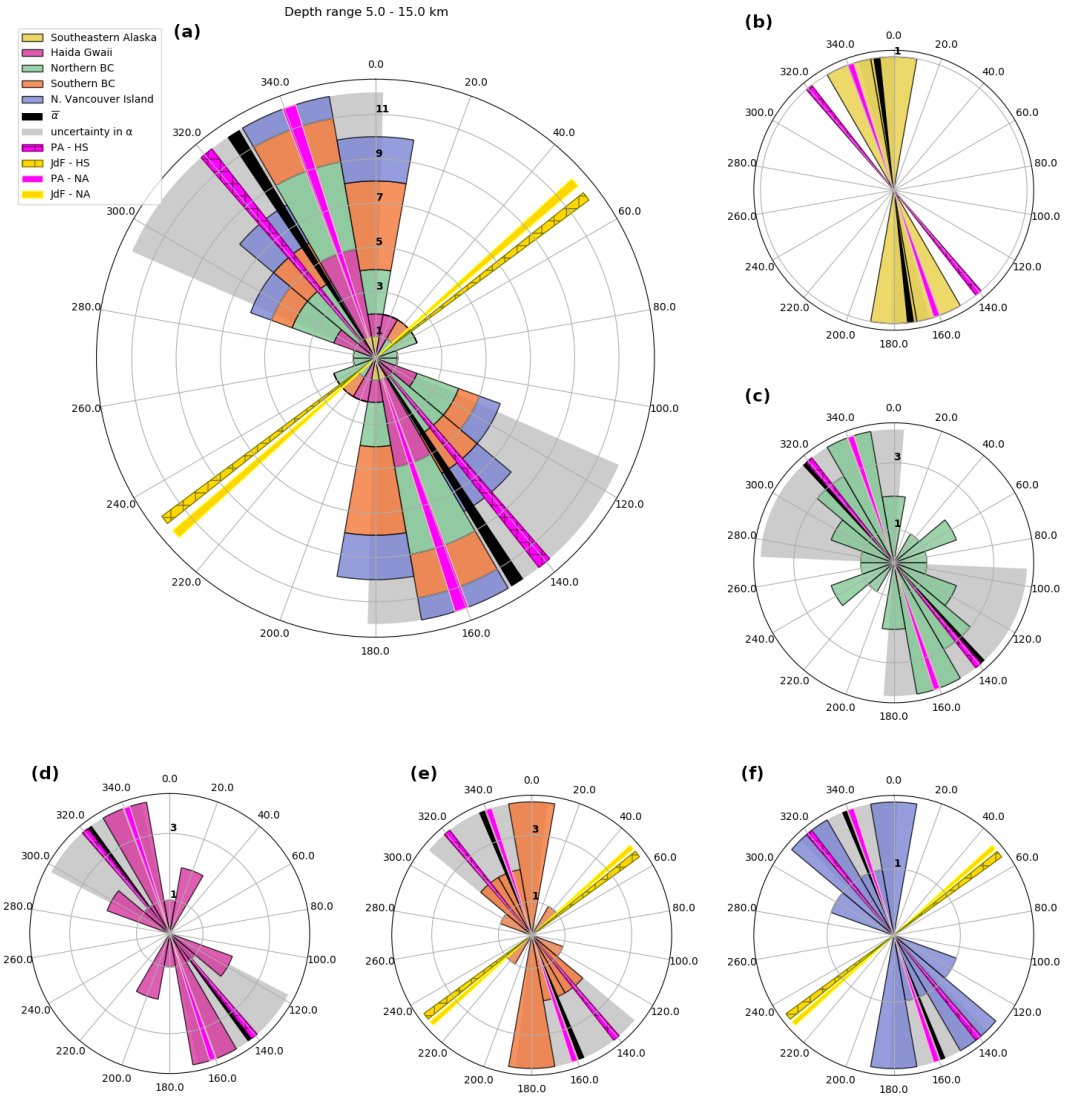

Figure 6. Rose diagrams showing the optimal orientations of the RFs for the 5 - 15 km depth range from Figure 4(a). Results are shown for (a) all stations, (b) southeastern Alaska, (c) Haida Gwaii, (d) northern BC, (e) southern BC, and (f) northern Vancouver Island. The circular mean angles are plotted as thick black lines with the standard deviation shown in light gray on each subplot. The directions of the PA and JdF plates relative to NA are plotted in pink and yellow respectively (Kreemer et al., 2014). The directions of the PA and JdF plates relative to the global hotspot reference frame are plotted with a hatch pattern in pink and yellow respectively (Gripp & Gordon, 2002).

smaller magnitudes. Stations on Haida Gwaii closer to the margin have larger magnitudes. Stations on northern Vancouver Island that lie past the approximate landward extent of the JdF slab have smaller magnitudes for most depth windows. Stations in southeastern Alaska have largest magnitudes for the 10 - 20 km and 20 - 30 km depth ranges.

5 Discussion

Anisotropy in RFs can arise from structural heterogeneity (e.g., dipping boundaries) and/or material anisotropy (Porter et al., 2011). These two sources of anisotropy produce similar signals in RF data and discriminating between them can prove challenging (Porter et al., 2011; Schulte-Pelkum & Mahan, 2014; Audet, 2015; Tarayoun et al., 2017), especially when both are present beneath a receiver. Structural heterogeneity caused by dipping structures at the km scale are expected in a geologically complex area such as the Haida Gwaii and Cascadia margins where large dipping faults exist, but also beneath major terrane boundaries in the form of Moho offsets or Moho dip, and as large-scale intrusions such as sill-like plutons (Rubin & Saleeby, 1992; Morozov et al., 2001; Hollister & Andronicos, 2006; Calkins et al., 2010). Material anisotropy is expected from pervasive micro-fracturing in the brittle crust due to the regional stress field (Crampin, 1994; Balfour et al., 2012), or through the coherent alignment of anisotropic minerals due to past or present deformation processes. Below we compare our anisotropy estimates with previous results and with expectations for both structural heterogeneity and material anisotropy. It should be noted that our analysis focuses on RF signatures due to anisotropy with a plunging axis of symmetry and/or dipping structures. Hence, this represents a possible source of discrepancy between our observations and previous studies that consider purely azimuthal anisotropy. We follow this conparison with a discussion of the implications of our observations for the structure of the crust in western Canada.

5.1 Comparison with previous anisotropy studies

RFs sample structure and anisotropy nearly vertically beneath recording stations. Other passive seismic methods that resolve crustal seismic anisotropy include shear-wave splitting from local earthquakes, and surface-wave tomography (at appropriate periods). Cao et al. (2017) estimated crustal seismic anisotropy using local shear-wave splitting estimated at five stations on Haida Gwaii. They generally found fast-axis directions subperpendicular to the maximum compressive stress direction, and attributed the crustal

anisotropy to structural fabrics arising from local geological features that have yet to be studied/identified. Interestingly, our results at the specific stations used by Cao et al. (2017) do not agree and show orientations either margin-parallel or sub-parallel to the maximum compressive stress (within the range of uncertainties) for our shallowest depth range. Such differences may arise from a number of effects, such as the averaging over a larger volume sampled by the regional S waves, the different depth sensitivity, and the small number of events considered in shear-wave splitting that resulted in only one well-constrained splitting estimate (Cao et al., 2017). This may suggest the presence of multiple sources of anisotropy and/or dipping structures beneath these sites.

Local shear-wave splitting was performed by Balfour et al. (2012) over the southern half of Vancouver Island and surrounding area. The splitting analysis from the majority of stations yielded a fast-axis aligned with the strike of the JdF-NA margin but results further northeast were approximately margin-perpendicular. These results were attributed to anisotropy in the upper crust caused by maximum compressive stress-aligned fluid-filled microcracks. Their results from stations along the western coast of Vancouver Island did not align with maximum compressive stress and instead were attributed to the long-term stress state caused by margin-parallel deformation. On the west coast of northern Vancouver Island, we find α aligned margin-parallel at shallow depths. Moving inland from the margin, the orientation of the fast-axis transitions to values similar to the maximum compressive stress direction (Balfour et al., 2011) but then rotates back towards margin-parallel, in agreement with Balfour et al. (2012). The margin-parallel stresses $\sim$150 km east of the margin reflects the residual strain caused by the northward push of the rotating Oregon Block (Balfour et al., 2012).

Gosselin et al. (2020) mapped the fast-axis orientation of azimuthal anisotropy from Rayleigh-wave group-velocity dispersion data over western Canada and northwestern United States. Fast-axis directions were found to be margin-parallel between Vancouver Island and Haida Gwaii. From the southeast to northwest they also observed a slight rotation and change in magnitude of fast-axis orientations. These results were consistent for Rayleigh-wave group velocity periods from 15 to 50 s, which are sensitive down to $\sim$80 km. The estimated fast-axis directions on Haida Gwaii were perpendicular to the maximum compressive stress found by Ristau et al. (2007) and thus attributed to structural foliations whereas fast-axis results elsewhere in the study region were attributed to maximum compressive stress-aligned fluid filled cracks and/or fabrics associated with tectonic assem-

bly of the margin. The observed rotation in anisotropy orientations between Vancouver Island and Haida Gwaii was attributed to the transitional tectonic regime along the coast (Gosselin et al., 2020). We observe this rotation in the dominant RF orientations in the 5 - 15 km and 25 - 35 km depth ranges only. Surface waves are sensitive to bulk properties integrated over a wide depth range (for a given period). It is likely that our RF analysis is sensitive to discontinuous structures as well as bulk properties that are also reflected in the surface wave data. Our results within 25 - 35 km depth likely encompasses the Moho, and is likely too deep to be attributable to crustal microcracks. Additionally, the results of the surface-wave study are obtained from a tomographic inversion with lower lateral resolution than our study at distinct individual stations.

5.2 Structural heterogeneity

Faults orientations taken from the BC Geological Survey's geology faults database (Cui, 2014) were compared to our results on a regional and local (< 5 km) scale. In general, α estimates do not consistently align with terrane boundaries or fault orientations (Fig. S2) at the majority of the depth ranges considered in this study. Instead, the average α estimates are rotated $>25^\circ$ clockwise from the average strike of mapped faults. Therefore, we interpret that fault structures do not represent the dominant source of BAZ variations in the RF data, but are a potential a contributing factor. Regionally, we expect dipping structures associated with deformation at active plate margins to dominate the RF signal, such as potential underthrusting beneath Haida Gwaii and northern Vancouver Island (Smith et al., 2003; Bustin et al., 2007; Audet et al., 2008; Gosselin et al., 2015), or across Moho depth gradients associated with the CPC (Morozov et al., 2001; Calkins et al., 2010).

Over Haida Gwaii, previous RF studies inferred an eastward increase in Moho depth from $\sim$18 km to 26 km (Smith et al., 2003; Bustin et al., 2007; Gosselin et al., 2015), in addition to a dipping interface from $\sim$25 km to 40 km potentially associated with PA slab underthrusting beneath the archipelago. Such dipping structures would be expected to generate RF anisotropy with α sub-parallel to the margin at those depths (Porter et al., 2011). However, the spatial distribution of α estimates across Haida Gwaii does not show this pattern except for the shallowest depth range, which does not encompass either of these dipping structures (Fig. 4(a), Figure 6). Based on Moho depth estimates, we should expect to see this signal between 15 km to 30 km (Fig.s 4(c) and (d)). Instead,

we see a juxtaposition of margin-parallel and margin-perpendicular α. Therefore, we do not attribute these signals in the RF data to arise from structural heterogeneity of a dipping Moho. At depth ranges associated with the underthrusting PA slab (25 km to 40 km, Figures 4(e) and (f)), we observe α orientations sub-parallel to the margin for the majority of stations on Haida Gwaii. Notably, stations further west have α aligned sub-perpendicular to the margin. At depths greater than 40 km (i.e., below the Moho), all stations except those at the very southern tip of Haida Gwaii resolve α perpendicular to the margin. These results support a layer dipping towards the northeast beginning at approximately 25 km depth (Smith et al., 2003; Bustin et al., 2007; Gosselin et al., 2015). Because these depths potentially encompass both the overriding plate and underthrusting material, RF signatures may reflect changes in material anisotropy above and below major tectonic contacts, as suggested by the observed rotations in the α values with depth (Fig. 4) and the presence of large variance in the $B_{\|}$ component of Figure 3(a).

On northern Vancouver Island, approximately half of the stations are located north of the terminus of the subducting JdF slab as determined by Audet et al. (2008). Due to the low dip angle of the JdF slab, α estimates are predicted to align with the slab strike as slab depth increases from 10 to 50 km below northern Vancouver Island. Above the JdF slab, α is rotated $\sim 0-20^{\circ}$ clockwise from the margin orientation and predicted slab strike, depending on the depth range considered. This could indicate an inaccurate slab depth model (Audet et al., 2008) and/or the contribution of material anisotropy above and below the JdF slab. North of the projected JdF slab, α estimates remain aligned with the margin and PA plate motion. However, we note that the relative magnitude of seismic anisotropy is lower in this region and some depth ranges display margin-normal orientations. This result is consistent with the absence of the JdF slab (Audet et al., 2008), and likely reflect the effects of material anisotropy in the crust.

In northern BC, V_p/V_s ratios measured by Calkins et al. (2010), and seismic reflectors identified by Morozov et al. (1998), indicate the presence of highly felsic sill-like plutons within the CPC and a Moho offset on the western boundary. Models proposed by Hollister and Andronicos (2006) and Morozov et al. (1998) account for this Moho offset with a thrust belt on the western edge of the CPC that extends to mantle depths. Their model also includes a ductile shear zone between the CPC and Stikinia terrane that dips east-to-northeast to a depth of $\sim$25 km below Stikinia and extends $>$50 km west of the boundary. Each of these structural heterogeneities may be reflected in our RF anal-

ysis. Along the eastern edge of the Alexander terrane (Fig. 1), α estimates are oriented NW-SE over all crustal depths but not below the predicted Moho depth. This supports the presence of a thrust belt through the entire crust. This feature persists into southeastern Alaska. We also note that this structure, which was suggested to have formed prior to the mid-Cretaceous translation of the terranes (Morozov et al., 1998), does not appear to be present in the YTT. At depths associated with the Moho, which dips northeast and increases west to east from ∼25 km to ∼30 km (Calkins et al., 2010), stations within the YTT and several stations in the Stikinia terrane have α values oriented N-S in contrast with the orientations in western Alexander terrane. Our limited dataset within the CPC, in addition to data from stations on the eastern edge of Stikinia, show a NE-SW alignment. For the northeast dipping Moho described by Calkins et al. (2010), we expect to see a NW-SE trend in the orientation of α values. However, outside of the Alexander terrane, our results display variable orientations in α at Moho depths. This may reflect complex local Moho topography rather than a consistent dipping Moho across the region. Furthermore, our results for the northern BC sub-region may be the result of a complex interplay between dipping structures from the Moho and plutons, in addition to seismically anisotropic materials.

Along the southern BC sub-region, Calkins et al. (2010) found that the Moho dips from a depth of ∼27 km in the west to ∼34 km in the east. Uncertainties in our analysis at Moho depths are significant (Fig. 4(d) and (e)). Two dominant orientations are present. However, it is challenging to identify spatial trends and the lack of high quality data prohibits us from further interpretation at Moho depths along the western boundary of the CPC. A dipping interface at ∼15 km depth between the CPC and Stikinia terrane was detected by Calkins et al. (2010) in southern BC, in agreement with the ductile shear zone in the model proposed by Hollister and Andronicos (2006). We observe the potential effects of a dipping interface in our α values for the southern BC sub-region for the 10-20 and 15-25 km depth ranges (Fig. 4(b) and (c)), where stations near the eastern edge of the CPC have α values aligned WNW-ESE, in contrast to other stations in the subset. This feature is challenging to identify in the northern BC sub-region due to a lack of high-quality data. Our results, in combination with Calkins et al. (2010), suggest that this dipping structure persists along the entire length of the boundary between the CPC and Stikinia.

5.3 Material anisotropy

Variations in the RF data with respect to BAZ are likely not explained solely by the effects of structural heterogeneity. In this section, we investigate models of material anisotropy in the crust to interpret our results. Because we estimate α from the degree-one harmonic term, we consider models that produce either a plunging slow-axis or plunging fast-axis of hexagonal symmetry (e.g. Porter et al., 2011). Continental seismic anisotropy typically originates from a combination of frozen (i.e., fossil) and active tectonics (Maupin & Park, 2007). Anisotropy in seismic waves can be caused by alternating layers with significant velocity contrasts (such as sediment stratigraphy); pervasive aligned cracks within an isotropic material; alignment of anisotropic minerals within a rock; or highly foliated metamorphic rocks. Here, we do not consider sediments as a significant source of anisotropy below 5 km depth. In the upper, brittle crust, azimuthal anisotropy (i.e., horizontal symmetry axis) is usually attributed to either mineral or (possibly fluid-filled) crack alignment. This is based on the closing of micro-fractures that are not aligned with the maximum principle stress axis (Crampin, 1994), which is sub-horizontal in western Canada (Ristau et al., 2007). Hexagonal anisotropy with a tilted axis in the mid- to lower-crust is believed to result from mineral alignment or foliated rocks such as mica schists (Porter et al., 2011). In the mantle, hexagonal anisotropy can arise from the coherent alignment of olivine in peridotite (fast symmetry axis) and/or serpentinite veins (slow symmetry axis) (Watanabe et al., 2007; Reynard, 2013). The source of the anisotropy in this study must be coherent at a scale resolvable by RFs (about 1-10 km).

In southern BC, along the eastern edge of the CPC, material anisotropy in the form of siliceous and foliated mylonites within the northeast dipping ductile shear zone (Jones & Nur, 1982; Heah, 1991; Andronicos et al., 2003) may also contribute to the WNW-ESE aligned α values in our results for the 10-20 and 15-25 km depth ranges (Fig. 4(b) and (c)) as the slow-axis of anisotropy.

In general, our α estimates for the shallowest depth range considered (5-15 km) do not align with the maximum horizontal stress directions. Therefore, we do not interpret our results to be the reflection of fluid-filled microcracks in this region. Given that α generally aligns well with the approximate strike of the QCF segment near Haida Gwaii, we attribute potential material anisotropy at shallow depths to shear-induced mineral alignment caused by the transpressive motion at the plate boundary. In the case of stations

with high uncertainty, the anisotropy measured may be a combination of shear-induced mineral alignments and stress oriented microcracks. Haida Gwaii and northern Vancouver Island both lie within the Wrangellia terrane, which is dominated by mafic and ultramafic rocks overlain by sediments (Shellnutt et al., 2021). Material anisotropy at upper crustal depths may also reflect pervasive fossil fabric from veining (or dykes), or shear-induced fabric acquired during margin-parallel translation of the terrane to its current location during the late Cretaceous to early Tertiary (Chardon et al., 1999; Hollister & Andronicos, 2006).

For many other locations throughout our study area, stress measurements are either sparse or unavailable, and we are not able to exclude stress-induced microcracks as a source of anisotropy at shallow depths. However, the stress field is expected to be relatively uniform throughout western Canada (Ristau et al., 2007), and this likely does not explain the observed scatter in α at short spatial scales. Our results do not show clustering with respect to surface geology (i.e., terrane boundaries). However, the average azimuths within the terranes are oriented $>25^{\circ}$ clockwise from the average strike of crustal faults (Fig. S2), which are attributed to the translation of the terranes along the margin. Therefore, we propose that the observed anisotropy may be caused by shear-induced mineral alignment during terrane emplacement (Chardon et al., 1999), which has been overprinted by the active tectonics in the region such as the slab window and the (poorly constrained) transition from subduction to transform plate boundaries from south to north (Gosselin et al., 2020).

6 Conclusions

RFs are calculated for a dataset of 74 land-based broadband seismic stations distributed around the Haida Gwaii margin, in order to study seismic anisotropy at crustal depths. The RF data vary with respect to BAZ, indicating the presence of seismic anisotropy or dipping structures beneath all stations considered here. These data are further processed to estimate a dominant orientation attributable to either the strike of a dipping interface or the trend of a plunging axis of material anisotropy.

At the shallowest depth, we observe a coherent orientation that rotates slightly along the strike of the margin from the southeast to the northwest. Beneath Haida Gwaii, our results agree with the presence of the underthrusting PA beneath NA. Beneath north-

ern Vancouver Island, we detect the effects of the subducting JdF slab, and are able to differentiate between stations that are above the slab and those beyond the northern extent of the JdF plate. Inland, we detect the signature of a thrust belt along the eastern boundary of the Alexander terrane. In southern BC, we detect either a dipping interface or material anisotropy caused by deformation between the CPC and Stikinia, which likely extends along the terrane boundary. Generally, dominant RF orientations are rotated clockwise from the strike of terrane boundaries and fault trends, and we attribute this to be the manifestation of fossil fabrics created during the translation of terranes overprinted by the modern active tectonics along the plate margins. The local complexity of our results highlights the complexity of this region.

This study adds additional constraint on seismic anisotropy throughout this complex geologic area, and provides insight into the formation of western BC and the current tectonic regime.

Acknowledgments

This project is supported by the Natural Sciences and Engineering Research Council of Canada Collaborative Research and Training Experience program (iMAGE-CREATE) on Marine Geodynamics and Georesources (TTK) and Discovery grant (PA), and a Vanier Canada Graduate Scholarship (JMG). Funding contributions have also made by the Canadian Exploration Geophysical Society (KEGS) foundation, the Canadian Society of Exploration Geophysicists (CSEG) and the Ontario Graduate Scholarship program (TTK). This work directly contributes to the objectives of the Geological Survey of Canada's Public Safety Geoscience Program, Plate Boundary Earthquakes and Active Tectonics Activity.

The seismic data used for RF processing in this study are available from IRIS Federation of Digital Seismograph Networks (FDSN) network identifiers for networks AT via doi: 10.7914/SN/AT (NOAA National Oceanic and Atmospheric Administration (USA), 1967), TA via doi: 10.7914/SN/TA (IRIS Transportable Array, 2003), and XY via doi: 10.7914/SN/XY_2005 (Dueker & Zandt, 2005) are available at www.iris.edu/hq/ and from the Canadian Hazards Information Service, Earthquakes Canada Database FDSN network identifiers CN via doi: 10.7914/SN/CN (Natural Resources Canada (NRCAN Canada), 1975) and C8 available at www.earthquakescanada.nrcan.gc.ca. A list of earthquake event metadata used in this study is available via doi: 10.5281/zenodo.6539941 (Tracey Kyryliuk

et al., 2022). v0.2.3 of StDb used for creation of station information databases licensed under Open copyright 2019 Andrew Schaeffer & Pascal Audet is freely available at schaefferaj.github.io/StDb. v0.1.0 of RfPy used for RF calculation and plotting, and harmonic decomposition and plotting, licensed under Open Copyright 2019 Pascal Audet is available at doi: 10.5281/zenodo.4302558 (Audet, 2020).

References

Andronicos, C. L., Chardon, D. H., Hollister, L. S., Gehrels, G. E., & Woodsworth, G. J. (2003). Strain partitioning in an obliquely convergent orogen, plutonism, and synorogenic collapse: Coast mountains batholith, british columbia, canada. *Tectonics*, *22*(2). Retrieved from `https://agupubs.onlinelibrary.wiley.com/doi/abs/10.1029/2001TC001312` doi: https://doi.org/10.1029/2001TC001312

Audet, P. (2015). Layered crustal anisotropy around the san andreas fault near parkfield, california. *Journal of Geophysical Research: Solid Earth*, *120*(5), 3527-3543. Retrieved from `https://agupubs.onlinelibrary.wiley.com/doi/abs/10.1002/2014JB011821` doi: https://doi.org/10.1002/2014JB011821

Audet, P. (2020). *Rfpy: Teleseismic receiver function calculation and post-processing.* Zenodo. Retrieved from `https://doi.org/10.5281/zenodo.4302558` doi: 10.5281/zenodo.4302558

Audet, P., Bostock, M. G., Mercier, J.-P., & Cassidy, J. F. (2008). Morphology of the Explorer–Juan de Fuca slab edge in northern Cascadia: Imaging plate capture at a ridge-trench-transform triple junction. *Geology*, *36*(11), 895–898.

Babuska, V., & Cara, M. (1991). *Seismic anisotropy in the earth* (Vol. 10). Springer Science & Business Media.

Balfour, N. J., Cassidy, J. F., & Dosso, S. E. (2012). Crustal anisotropy in the forearc of the Northern Cascadia Subduction Zone, British Columbia. *Geophysical Journal International*, *188*(1), 165-176. Retrieved from `https://doi.org/10.1111/j.1365-246X.2011.05231.x` doi: 10.1111/j.1365-246X.2011.05231.x

Balfour, N. J., Cassidy, J. F., Dosso, S. E., & Mazzotti, S. (2011). Mapping crustal stress and strain in southwest British Columbia. *Journal of Geophysical Research*, *116*, B03314. Retrieved from `https://hal.archives-ouvertes.fr/`

hal-00853734 doi: 10.1029/2010JB008003

Bianchi, I., Park, J., Piana Agostinetti, N., & Levin, V. (2010). Mapping seismic anisotropy using harmonic decomposition of receiver functions: An application to northern apennines, italy. *Journal of Geophysical Research: Solid Earth*, *115*(B12). Retrieved from https://agupubs.onlinelibrary.wiley.com/doi/abs/10.1029/2009JB007061 doi: https://doi.org/10.1029/2009JB007061

Bird, A. L. (1999). *Earthquakes in the queen charlotte islands region, 1982-1996* (Unpublished doctoral dissertation). National Library of Canada = Bibliotheque nationale du Canada.

Bustin, A. M. M., Hyndman, R. D., Kao, H., & Cassidy, J. F. (2007). Evidence for underthrusting beneath the Queen Charlotte Margin, British Columbia, from teleseismic receiver function analysis. *Geophysical Journal International*, *171*(3), 1198-1211. Retrieved from https://doi.org/10.1111/j.1365-246X.2007.03583.x doi: 10.1111/j.1365-246X.2007.03583.x

Calkins, J. A., Zandt, G., Girardi, J., Dueker, K., Gehrels, G. E., & Ducea, M. N. (2010). Characterization of the crust of the coast mountains batholith, british columbia, from p to s converted seismic waves and petrologic modeling. *Earth and Planetary Science Letters*, *289*(1), 145-155. Retrieved from https://www.sciencedirect.com/science/article/pii/S0012821X09006463 doi: https://doi.org/10.1016/j.epsl.2009.10.037

Canadian Hazards Information Service. (2021). velocity model vel06 (continental haida gwaii) used for the national earthquake database.

Cao, L., Kao, H., & Wang, K. (2017). Contrasting upper-mantle shear wave anisotropy across the transpressive queen charlotte margin. *Tectonophysics*, *717*, 311-320. Retrieved from https://www.sciencedirect.com/science/article/pii/S0040195117303074 doi: https://doi.org/10.1016/j.tecto.2017.07.025

Cassidy, J. F. (1992). Numerical experiments in broadband receiver function analysis. *Bulletin of the Seismological Society of America*, *82*, 1453—1474.

Cassidy, J. F., Rogers, G. C., & Hyndman, R. D. (2014). An overview of the 28 october 2012 m w 7.7 earthquake in haida gwaii, canada: a tsunamigenic thrust event along a predominantly strike-slip margin. *Pure and Applied Geophysics*, *171*(12), 3457–3465.

Chardon, D., Andronicos, C. L., & Hollister, L. S. (1999). Large-scale transpressive shear zone patterns and displacements within magmatic arcs: The coast plutonic complex, british columbia. *Tectonics*, *18*(2), 278—292. doi: 10.1029/1998TC900035

Cook, F., White, D., Jones, A., Eaton, D., Hall, J., & Clowes, R. (2010). How the crust meets the mantle: Lithoprobe perspectives on the mohorovii discontinuity and crust-mantle transition. *Canadian Journal of Earth Sciences*, *47*, 315-351. doi: 10.1139/E09-076

Crampin, S. (1994). The fracture criticality of crustal rocks. *Geophysical Journal International*, *118*(2), 428-438. Retrieved from `https://onlinelibrary.wiley.com/doi/abs/10.1111/j.1365-246X.1994.tb03974.x` doi: https://doi.org/10.1111/j.1365-246X.1994.tb03974.x

Cui, Y. (2014). (2018th ed.). Retrieved from `https://catalogue.data.gov.bc.ca/dataset/geology-faults`

DeMets, C., & Dixon, T. H. (1999). New kinematic models for pacific-north america motion from 3 ma to present, i: Evidence for steady motion and biases in the nuvel-1a model. *Geophysical Research Letters*, *26*(13), 1921-1924. Retrieved from `https://agupubs.onlinelibrary.wiley.com/doi/abs/10.1029/1999GL900405` doi: https://doi.org/10.1029/1999GL900405

DeMets, C., Gordon, R. G., & Argus, D. F. (2010). Geologically current plate motions. *Geophysical Journal International*, *181*(1), 1-80. Retrieved from `https://doi.org/10.1111/j.1365-246X.2009.04491.x` doi: 10.1111/j.1365-246X.2009.04491.x

Dueker, K., & Zandt, G. (2005). *Magma accretion and the formation of batholiths.* International Federation of Digital Seismograph Networks. Retrieved from `https://www.fdsn.org/networks/detail/XY_2005/` doi: 10.7914/SN/XY_2005

Engebretson, D. C., Cox, A., & Gordon, R. G. (1984). Relative motions between oceanic plates of the pacific basin. *Journal of Geophysical Research: Solid Earth*, *89*(B12), 10291-10310. Retrieved from `https://agupubs.onlinelibrary.wiley.com/doi/abs/10.1029/JB089iB12p10291` doi: https://doi.org/10.1029/JB089iB12p10291

Gabrielse, H., Monger, J. W. H., Wheeler, J. O., & Yorath, C. J. (1991). Part a:

Morphogeological belts, tectonic assemblages and terranes [chapter 2: Tectonic framework]. In (Vol. G-2, p. 15/28). doi: https://doi.org/10.4095/134069

Gosselin, J. M., Audet, P., Schaeffer, A. J., Darbyshire, F. A., & Estève, C. (2020). Azimuthal anisotropy in Bayesian surface wave tomography: application to northern Cascadia and Haida Gwaii, British Columbia. *Geophysical Journal International*, *224*(3), 1724-1741. Retrieved from `https://doi.org/10.1093/gji/ggaa561` doi: 10.1093/gji/ggaa561

Gosselin, J. M., Cassidy, J. F., & Dosso, S. E. (2015). Shear-wave velocity structure in the vicinity of the 2012 mw 7.8 haida gwaii earthquake from receiver function inversion. *Bulletin of the Seismological Society of America*, *105*(2B), 1106–1113. doi: 10.1785/0120140171

Gripp, A. E., & Gordon, R. G. (2002). Young tracks of hotspots and current plate velocities. *Geophysical Journal International*, *150*(2), 321-361. Retrieved from `https://doi.org/10.1046/j.1365-246X.2002.01627.x` doi: 10.1046/j.1365-246X.2002.01627.x

Hammer, P. T.-C., Clowes, R. M., & Ellis, R. M. (2000). Crustal structure of NW British Columbia and SE Alaska from seismic wide-angle studies: Coast Plutonic Complex to Stikinia. *JGR*, *105*(B4), 7961-7981. doi: 10.1029/1999JB900378

Heah, T. S. T. (1991). Mesozoic ductile shear and paleogene extension along the eastern margin of the central gneiss complex, coast belt, shames river area, near terrace, british columbia..

Hollister, L. S., & Andronicos, C. L. (2006). Formation of new continental crust in western british columbia during transpression and transtension. *Earth and Planetary Science Letters*, *249*(1), 29-38. Retrieved from `https://www.sciencedirect.com/science/article/pii/S0012821X06004857` doi: https://doi.org/10.1016/j.epsl.2006.06.042

Hyndman, R. D. (2015). Tectonics and structure of the queen charlotte fault zone, haida gwaii, and large thrust earthquakes. *Bulletin of the Seismological Society of America*, *105*(2B), 1058–1075.

Hyndman, R. D., & Ellis, R. M. (1981). Queen charlotte fault zone: microearthquakes from a temporary array of land stations and ocean bottom seismographs. *Canadian Journal of Earth Sciences*, *18*(4), 776-788. Retrieved

from https://doi.org/10.1139/e81-071 doi: 10.1139/e81-071

IRIS Transportable Array. (2003). *Usarray transportable array.* International Federation of Digital Seismograph Networks. Retrieved from https://www.fdsn.org/networks/detail/TA/ doi: 10.7914/SN/TA

Jones, T., & Nur, A. (1982). Seismic velocity and anisotropy in mylonites and the reflectivity of deep crystal fault zones. *Geology*, *10*(5), 260. doi: 10.1130/0091-7613(1982)10\textless{}260:SVAAIM\textgreater{}2.0.CO;2

Kennett, B. L. N., & Engdahl, E. R. (1991). *iasp91 velocity model.* Retrieved from www.iaspei.org/projects/projects.html doi: https://doi.org/10.17611/DP/9991809

Kreemer, C., Blewitt, G., & Klein, E. C. (2014). A geodetic plate motion and global strain rate model. *Geochemistry, Geophysics, Geosystems*, *15*(10), 3849-3889. Retrieved from https://agupubs.onlinelibrary.wiley.com/doi/abs/10.1002/2014GC005407 doi: https://doi.org/10.1002/2014GC005407

Langston, C. A. (1977). The effect of planar dipping structure on source and receiver responses for constant ray parameter. *Bulletin of the Seismological Society of America*, *67*(4), 1029-1050. Retrieved from https://doi.org/10.1785/BSSA0670041029 doi: 10.1785/BSSA0670041029

Langston, C. A. (1979). Structure under mount rainier, washington, inferred from teleseismic body waves. *Journal of Geophysical Research: Solid Earth*, *84*(B9), 4749-4762. Retrieved from https://agupubs.onlinelibrary.wiley.com/doi/abs/10.1029/JB084iB09p04749 doi: https://doi.org/10.1029/JB084iB09p04749

Lay, T., Ye, L., Kanamori, H., Yamazaki, Y., Cheung, K. F., Kwong, K., & Koper, K. D. (2013). The october 28, 2012 mw 7.8 haida gwaii underthrusting earthquake and tsunami: Slip partitioning along the queen charlotte fault transpressional plate boundary. *Earth and Planetary Science Letters*, *375*, 57-70. Retrieved from https://www.sciencedirect.com/science/article/pii/S0012821X13002434 doi: https://doi.org/10.1016/j.epsl.2013.05.005

Leonard, L., & Bednarski, J. (2014). Field survey following the 28 october 2012 haida gwaii tsunami. *Pure and Applied Geophysics*, *171*(12), 3467–3482.

Levin, V., & Park, J. (1997). Crustal anisotropy in the ural mountains foredeep from teleseismic receiver functions. *Geophysical Research Letters*, *24*(11),

1283–1286.

Maupin, V., & Park, J. (2007). 1.09 - theory and observations – wave propagation in anisotropic media. In G. Schubert (Ed.), *Treatise on geophysics* (p. 289-321). Amsterdam: Elsevier. Retrieved from https://www.sciencedirect.com/science/article/pii/B9780444527486000079 doi: https://doi.org/10.1016/B978-044452748-6.00007-9

McCaffrey, R., Long, M. D., Goldfinger, C., Zwick, P. C., Nabelek, J. L., Johnson, C. K., & Smith, C. (2000). Rotation and plate locking at the southern cascadia subduction zone. *Geophysical Research Letters*, *27*(19), 3117-3120. Retrieved from https://agupubs.onlinelibrary.wiley.com/doi/abs/10.1029/2000GL011768 doi: https://doi.org/10.1029/2000GL011768

Monger, J. W. H. (1993). Canadian cordilleran tectonics: from geosynclines to crustal collage. *Canadian Journal of Earth Sciences*, *30*(2), 209-231. Retrieved from https://doi.org/10.1139/e93-019 doi: 10.1139/e93-019

Morozov, I. B., Smithson, S. B., Chen, J., & Hollister, L. S. (2001). Generation of new continental crust and terrane accretion in southeastern alaska and western british columbia: constraints from p- and s-wave wide-angle seismic data (accrete). *Tectonophysics*, *341*(1), 49-67. Retrieved from https://www.sciencedirect.com/science/article/pii/S0040195101001901 doi: https://doi.org/10.1016/S0040-1951(01)00190-1

Morozov, I. B., Smithson, S. B., Hollister, L. S., & Diebold, J. B. (1998). Wide-angle seismic imaging across accreted terranes, southeastern alaska and western british columbia. *Tectonophysics*, *299*(4), 281-296. Retrieved from https://www.sciencedirect.com/science/article/pii/S004019519800208X doi: https://doi.org/10.1016/S0040-1951(98)00208-X

Natural Resources Canada (NRCAN Canada). (1975). *Canadian national seismograph network.* International Federation of Digital Seismograph Networks. Retrieved from https://www.fdsn.org/networks/detail/CN/ doi: 10.7914/SN/CN

Nelson, J. L., Colpron, M., & Goodfellow, W. D. (2007). Tectonics and metallogeny of the british columbia, yukon and alaskan cordillera, 1.8 ga to the present. *Mineral deposits of Canada: A synthesis of major deposit-types, District Metallogeny, the evolution of geological provinces, and exploration methods: Geolog-*

ical Association of Canada, Mineral Deposits Division, Special Publication, *5*, 755–791.

Nelson, J. L., Colpron, M., Israel, S., Bissig, T., Rusk, B. G., & Thompson, J. F. H. (2013). The cordillera of british columbia, yukon, and alaska: tectonics and metallogeny. *Tectonics, Metallogeny, and Discovery: The North American Cordillera and Similar Accretionary Settings: Society of Economic Geologists Special Publication*, *17*, 53–109.

NOAA National Oceanic and Atmospheric Administration (USA). (1967). *National tsunami warning center alaska seismic network.* International Federation of Digital Seismograph Networks. Retrieved from `https://www.fdsn.org/networks/detail/AT/` doi: 10.7914/SN/AT

Park, J., & Levin, V. (2000). Receiver Functions from Multiple-Taper Spectral Correlation Estimates. *Bulletin of the Seismological Society of America*, *90*(6), 1507-1520. Retrieved from `https://doi.org/10.1785/0119990122` doi: 10.1785/0119990122

Porter, R., Zandt, G., & McQuarrie, N. (2011). Pervasive lower-crustal seismic anisotropy in Southern California: Evidence for underplated schists and active tectonics. *Lithosphere*, *3*(3), 201-220. Retrieved from `https://doi.org/10.1130/L126.1` doi: 10.1130/L126.1

Reynard, R. (2013). Serpentine in active subduction zones. *Lithos*, *178*, 171-185. Retrieved from `https://www.sciencedirect.com/science/article/pii/S002449371200432X` (Serpentinites from mid-oceanic ridges to subduction) doi: https://doi.org/10.1016/j.lithos.2012.10.012

Ristau, J., Rogers, G. C., & Cassidy, J. F. (2007). Stress in western canada from regional moment tensor analysis. *Canadian Journal of Earth Sciences*, *44*(2), 127-148. Retrieved from `https://www.scopus.com/inward/record.uri?eid=2-s2.0-34249696881&doi=10.1139%2fE06-057&partnerID=40&md5=5ee53cf96e158ac78fa0b51c5c6bffb8` (cited By 60) doi: 10.1139/E06-057

Rohr, K. M. M., Scheidhauer, M., & Trehu, A. M. (2000). Transpression between two warm mafic plates: The queen charlotte fault revisited. *Journal of Geophysical Research: Solid Earth*, *105*(B4), 8147-8172. Retrieved from `https://agupubs.onlinelibrary.wiley.com/doi/abs/10.1029/1999JB900403` doi:

https://doi.org/10.1029/1999JB900403

Rubin, C. M., & Saleeby, J. B. (1992). Tectonic history of the eastern edge of the Alexander Terrane, southeast Alaska. *Tectonics*, *11*(3), 586-602. doi: 10.1029/91TC02182

Savage, M. K. (1998a). Lower crustal anisotropy or dipping boundaries? effects on receiver functions and a case study in new zealand. *Journal of Geophysical Research: Solid Earth*, *103*(B7), 15069–15087.

Savage, M. K. (1998b). Lower crustal anisotropy or dipping boundaries? effects on receiver functions and a case study in new zealand. *Journal of Geophysical Research: Solid Earth*, *103*(B7), 15069-15087. Retrieved from `https://agupubs.onlinelibrary.wiley.com/doi/abs/10.1029/98JB00795` doi: https://doi.org/10.1029/98JB00795

Savard, G., Bostock, M. G., Hutchinson, J., Kao, H., Christensen, N. I., & Peacock, S. M. (2020). The northern terminus of cascadia subduction. *Journal of Geophysical Research: Solid Earth*, *125*(6), e2019JB018453. Retrieved from `https://agupubs.onlinelibrary.wiley.com/doi/abs/10.1029/2019JB018453` (e2019JB018453 10.1029/2019JB018453) doi: https://doi.org/10.1029/2019JB018453

Schoettle-Greene, P., Duvall, A. R., Blythe, A., Morley, E., Matthews, W., & LaHusen, S. R. (2020). Uplift and exhumation in Haida Gwaii driven by terrane translation and transpression along the southern Queen Charlotte fault, Canada. *Geology*, *48*(9), 908-912. Retrieved from `https://doi.org/10.1130/G47364.1` doi: 10.1130/G47364.1

Schulte-Pelkum, V., & Mahan, K. H. (2014). A method for mapping crustal deformation and anisotropy with receiver functions and first results from usarray. *Earth and Planetary Science Letters*, *402*, 221-233. Retrieved from `https://www.sciencedirect.com/science/article/pii/S0012821X14000661` (Special issue on USArray science) doi: https://doi.org/10.1016/j.epsl.2014.01.050

Shellnutt, J. G., Dostal, J., & Lee, T. Y. (2021). Linking the wrangellia flood basalts to the galápagos hotspot. *Scientific Reports*, *11*(8579). Retrieved from `https://doi.org/10.1038/s41598-021-88098-7` doi: 10.1038/s41598-021-88098-7

Smith, A. J., Hyndman, R. D., Cassidy, J. F., & Wang, K. (2003). Structure, seis-

micity, and thermal regime of the queen charlotte transform margin. *Journal of Geophysical Research: Solid Earth*, *108*(B11). Retrieved from https://agupubs.onlinelibrary.wiley.com/doi/abs/10.1029/2002JB002247 doi: https://doi.org/10.1029/2002JB002247

Tarayoun, A., Audet, P., Mazzotti, S., & Ashoori, A. (2017). Architecture of the crust and uppermost mantle in the northern Canadian Cordillera from receiver functions. *Journal of Geophysical Research : Solid Earth*, *122*(7), 5268-5287. Retrieved from https://hal.archives-ouvertes.fr/hal-01685550 doi: 10.1002/2017JB014284

ten Brink, U. S., Miller, N. C., Andrews, B. D., Brothers, D. S., & Haeussler, P. J. (2018). Deformation of the pacific/north america plate boundary at queen charlotte fault: The possible role of rheology. *Journal of Geophysical Research: Solid Earth*, *123*(5), 4223-4242. Retrieved from https://agupubs.onlinelibrary.wiley.com/doi/abs/10.1002/2017JB014770 doi: https://doi.org/10.1002/2017JB014770

Thorkelson, D. J., Madsen, J. K., & Sluggett, C. L. (2011). Mantle flow through the Northern Cordilleran slab window revealed by volcanic geochemistry. *Geology*, *39*(3), 267-270. Retrieved from https://doi.org/10.1130/G31522.1 doi: 10.1130/G31522.1

Thorkelson, D. J., & Taylor, R. P. (1989). Cordilleran slab windows. *Geology*, *17*(9), 833-836. Retrieved from https://doi.org/10.1130/0091-7613(1989)017<0833:CSW>2.3.CO;2 doi: 10.1130/0091-7613(1989)017⟨0833:CSW⟩2.3.CO;2

Tracey Kyryliuk, T., Audet, P., Gosselin, J. M., & Schaeffer, A. J. (2022). *Event Data used in Seismic anisotropy along the Haida Gwaii margin from receiver function analysis.* Zenodo. Retrieved from https://doi.org/10.5281/zenodo.6539941 doi: 10.5281/zenodo.6539941

Watanabe, T., Kasami, H., & Ohshima, S. (2007, 04). Compressional and shear wave velocities of serpentinized peridotites up to 200 mpa. *Earth Planets Space*, *59*, 233-244. doi: 10.1186/BF03353100